Supplementary Information for

Ultrahigh thermal conductance between III-nitride semiconductor and diamond via interfacial atomic reordering

Beile Chen[1,8], Nianjie Liang[2,8], Hongcai Yang[1,8], Zifeng Huang[3,8], Xuelin Yang[1,7] ✉, Kexin Zhang[1], Han Yang[1], Haichang Guo[2], Wujuan Yan[2], Yuxi Wang[2], Guangxu Ju[1,7], Fujun Xu[1,7], Ning Tang[1,7], Xinqiang Wang[1,7], Weikun Ge[1], Jinlong Du[4], Zhe Cheng[3], Peng Gao[4, 5], Bai Song[2,6, ✉], Bo Shen[1,7,8, ✉]

[1]State Key Laboratory for Mesoscopic Physics and Frontiers Science Center for Nano-optoelectronics, School of Physics, Peking University, Beijing 100871, China.

[2]School of Mechanics and Engineering Science, Peking University, Beijing 100871, China.

[3]School of Integrated Circuits and Beijing Advanced Innovation Center for Integrated Circuits, Peking University, Beijing 100871, China.

[4]Electron Microscopy Laboratory, School of Physics, Peking University, Beijing 100871, China.

[5]International Center for Quantum Materials, School of Physics, Peking University, Beijing 100871, China.

[6]National Key Laboratory of Advanced Micro and Nano Manufacture Technology, Beijing 100871, China.

[7]Beijing Key Laboratory of Nitride Wide Bandgap Semiconductor Materials and Devices, School of Physics, Peking University, Beijing 100871, China.

[8]Collaborative Innovation Center of Quantum Matter, Beijing 100871, China.

[9]These authors contributed equally: Beile Chen, Nianjie Liang, Hongcai Yang, Zifeng Huang.

✉e-mail: xlyang@pku.edu.cn; songbai@pku.edu.cn; bshen@pku.edu.cn

This PDF file includes:

Supplementary Methods
Supplementary Figs. 1 to 20
Supplementary Tables 1 to 4
References

Supplementary Methods

1. High-resolution X-ray diffraction

High-resolution X-ray diffraction (XRD) measurements were performed using the Philips PANalytical X'pert XRD system to assess the crystalline quality of AlN. XRD φ-scans were specifically conducted on the AlN $(10\bar{1}2)$ plane (Supplementary Fig. 3a). The six pronounced peaks separated by 60° intervals confirm the hexagonal structure and highly uniform in-plane orientation of the AlN layers. Furthermore, the high crystal quality of AlN layers was evidenced by the narrow full width at half maximum (FWHM) of 0.85° for the AlN (0002) rocking curve (Supplementary Fig. 3b).

2. Atomic force microscopy

The surface morphology of the AlN layer was characterized using tapping-mode atomic force microscopy (AFM) on a Bruker Dimension ICON system, as depicted in Supplementary Fig. 2. The root-mean-square (RMS) roughness of the GaN layer, measured over a 5 μm×5 μm area, was found to be less than 0.67 nm.

3. Time-domain thermoreflectance

The Time-domain thermoreflectance (TDTR) measurements were performed on our two-color platform[1] at the two modulation frequencies of 5.02 MHz and 10.00 MHz at Peking University and also double checked by a two-tint system[2] with a modulation frequency of 10.1 MHz at Tsinghua Shenzhen International Graduate School. The corner of the sample which was not coated with AlN was first used to determine the thermal conductivity of the diamond substrate ($\kappa_{\mathrm{Diamond}}$). The fitting curves of $\kappa_{\mathrm{Diamond}}$

are shown in Fig. 3b and Supplementary Fig. 8, yielding a value of 2180 $Wm^{-1}K^{-1}$, which is close to the literature values[3-5]. The measured diamond thermal conductivity is used in the subsequent data fitting procedure for the AlN/Diamond sample, and the fitting parameters are listed in Supplementary Table 1 where three unknown parameters, $G_{Al/AlN}$, κ_{AlN}, and $G_{AlN/Diamond}$, were extracted. The representative experimental data and fitting results for the sample with an AlN layer thickness of 230 nm, measured using the two-color system, are shown in Fig. 3b (with modulation frequency of 5.02 MHz) and Supplementary Fig. 10a. The lower bound of $G_{AlN/Diamond}$ was estimated by fixing one parameter, κ_{AlN}, to an upper bound of 100 $Wm^{-1}K^{-1}$, based on the theoretical calculations in literature[6]. Repeating the fitting process, we found that $G_{AlN/Diamond}$ should be no less than 700 $MWm^{-2}K^{-1}$ (Supplementary Fig. 9).

The sensitivity S of the TDTR signal to a parameter α is determined by[7]:

$$S_\alpha = \frac{\partial \ln\left(-\frac{V_{\text{in}}}{V_{\text{out}}}\right)}{\partial \ln(\alpha)}, \quad \text{(S1)}$$

Parameters with higher sensitivity can be measured with greater accuracy. The sensitivity plots for the sample with an AlN layer thickness of 230 nm and the modulation frequencies of 5.02 MHz and 10.00 MHz are shown in Supplementary Fig. 11.

In order to further confirm the high $G_{AlN/Diamond}$, an additional sample with an AlN layer thickness of 150 nm was prepared and tested by the two-tint system (Supplementary Fig. 12a). The thermal conductivity of the AlN layer varied, which is attributed to the thickness dependence of κ_{AlN} due to boundary scattering (the fitting

parameters are listed in Supplementary Table 2)[8]. However, the fitting result of $G_{AlN/Diamond}$ is 870 $MWm^{-2}K^{-1}$, which is very close to the result shown in Fig. 3b. The sensitivity plot for this sample with a modulation frequency of 10.1 MHz are shown in Supplementary Fig. 12b.

4. Frequency-domain thermoreflectance

The sensitivity S_x of the FDTR signal to a parameter x can be defined as the phase difference caused by a certain amount of (say ±10%) variations in x: $S_{x,10\%}(\omega) = \varphi_{1.1x}(\omega) - \varphi_{0.9x}(\omega)$, as shown in Supplementary Fig. 13a. Based on the sensitivity curves, the interfacial thermal conductance between Au and AlN ($G_{Au/AlN}$) shows the highest sensitivity, and therefore can be accurately measured and is fitted to be 58 $MWm^{-2}K^{-1}$ according to Supplementary Fig. 13c. The thermal conductivity of AlN (κ_{AlN}) has a lower sensitivity and is initially assumed to be 65 $Wm^{-1}K^{-1}$ based on the TDTR results, which is also consistent with previous reports considering the thickness and grain size of the AlN layers [8]. Once κ_{AlN} and $G_{Au/AlN}$ were set, the experimental data can be fitted well when the interfacial thermal conductance between AlN and diamond ($G_{AlN/Diamond}$) is 900 $MWm^{-2}K^{-1}$ (the fitting parameters are listed in Supplementary Table 3).

A notable deviation between the fitted curve and experimental data can be observed when $G_{AlN/Diamond}$ was 600 $MWm^{-2}K^{-1}$, suggesting that the interfacial thermal conductance should be no less than 600 $MWm^{-2}K^{-1}$. To further elucidate this, a contour map of the root-mean-square error (RMSE) between the fitted and experimental data for different κ_{AlN} is plotted. As shown in Supplementary Fig. 13e, the dark blue region indicates the lowest RMSE value when $G_{Au/AlN}$ is ~58 $MWm^{-2}K^{-1}$, and $G_{AlN/Diamond}$

ranges from ~600 $MWm^{-2}K^{-1}$ to ~1000 $MWm^{-2}K^{-1}$, which is consistent with Supplementary Fig. 13b,c. If κ_{AlN} is set to 50 $Wm^{-1}K^{-1}$ (Supplementary Fig. 13d), $G_{AlN/Diamond}$ would exceed 900 $MWm^{-2}K^{-1}$. Similarly, if κ_{AlN} is assumed to reach the upper bound of 100 $Wm^{-1}K^{-1}$, the region with the smallest RMSE still suggests a high $G_{AlN/Diamond}$ over 600 $MWm^{-2}K^{-1}$ (Supplementary Fig. 13f). Taken together, these results confirm the ultrahigh interfacial thermal conductance between AlN and diamond, which is approximately 900 $MWm^{-2}K^{-1}$, consistent with the TDTR results.

5. Training the neuroevolution potential model

We constructed AlN ($000\bar{1}$)/Diamond (111) interface models with and without the substitution of some C atoms by N atoms (N_C), each containing 184 atoms. The AlN lattice was rotated by 60° to match that of the diamond. Then the structures were relaxed for both lattice constants and atomic positions using the CP2K package[9]. Based on the relaxed structures, we performed *ab initio* molecular dynamics (AIMD) simulations under an isothermal-isobaric (NPT) ensemble to prepare the training and test datasets. A total of 2710 configurations, spanning temperatures from 100 K to 1200 K, were generated for both cases. Among them, 2304 configurations were used to prepare the training dataset, while 406 were allocated for the test dataset.

Density functional theory (DFT) calculations were conducted using the CP2K package[9] to obtain the energies, forces, and virial stresses for these structures in the datasets, with periodic boundary conditions (PBC) applied in all directions. The Perdew-Burke-Ernzerhof (PBE) functional with the generalized gradient approximation[10] and the DZVP-MOLOPT-SR-GTH basis set[11] were employed, along

with the Geodecker-Teter-Hutter (GTH) pseudopotentials[12] to describe the ion-electron interactions. Dispersion corrections DFT-D3 with the Becke Johnson damping function[13,14] were included. A cutoff energy of 700 Ry was used, and the energy convergence criterion was 10^{-7} hartree. The **k**-points were set to 4×7×1.

The neuroevolution potential (NEP) models[15-17] for the interface with and without N_C were trained using the Graphics Processing Units Molecular Dynamics (GPUMD) package[18-20]. The cutoff radii of the radial and angular descriptor components were set to 6.5 Å and 5 Å, respectively. The number of descriptor components and basis functions for the radial and angular descriptors were all set to 8. The training involved 150000 generations, while other parameters used default values. The training results are shown in Supplementary Fig. 19. The low RMSE of energy, force, and virial stress for both models demonstrate the high accuracy of the NEP model.

6. Interfacial vibration modes

Vibrations in the interfacial region tend to be rather complex. The atomic vibrations near the AlN/Diamond interface consist of contributions from four sources: the characteristic bulk modes of AlN, those of diamond, localized vibrational modes due to the presence of the interface (lack of lattice translation symmetry), and the localized modes caused by N_C on the diamond side. Based on a state-of-the-art approach[21-23], the effects of the bulk vibrational modes on the two sides of the interface can be subtracted by minimizing the difference between the overall spectrum and all possible linear combinations of the two bulk spectra. The fitting is performed by minimizing the residual:

$$\text{Residual} = \sum_{\omega} \|S(\omega) - a_1 S_{\text{Diamond}}(\omega) - a_2 S_{\text{AlN}}(\omega)\| \quad \text{(S2)}$$

where $S(\omega)$ is the overall spectrum in the interfacial region, $S_{\text{Diamond}}(\omega)$ and $S_{\text{AlN}}(\omega)$ are the bulk spectra of diamond and AlN, respectively, and a_1 and a_2 are the coefficients to be determined.

After removing the bulk contributions via residual analysis, it is also necessary to further distinguish between the contribution from the lack of translation symmetry and the impact of N_C. This is achieved by comparing the results of residual calculations for the atomic structures with and without N_C. The role of the localized vibrational modes associated solely with the N_C in phonon transport across the AlN/Diamond interface can then be analyzed.

The phonon eigenvectors were calculated using GPUMD with the finite-displacement method for small models containing 3872 atoms, both with and without N_C. For clarity, only partial structures are visualized in Fig. 5a.

Supplementary Figures

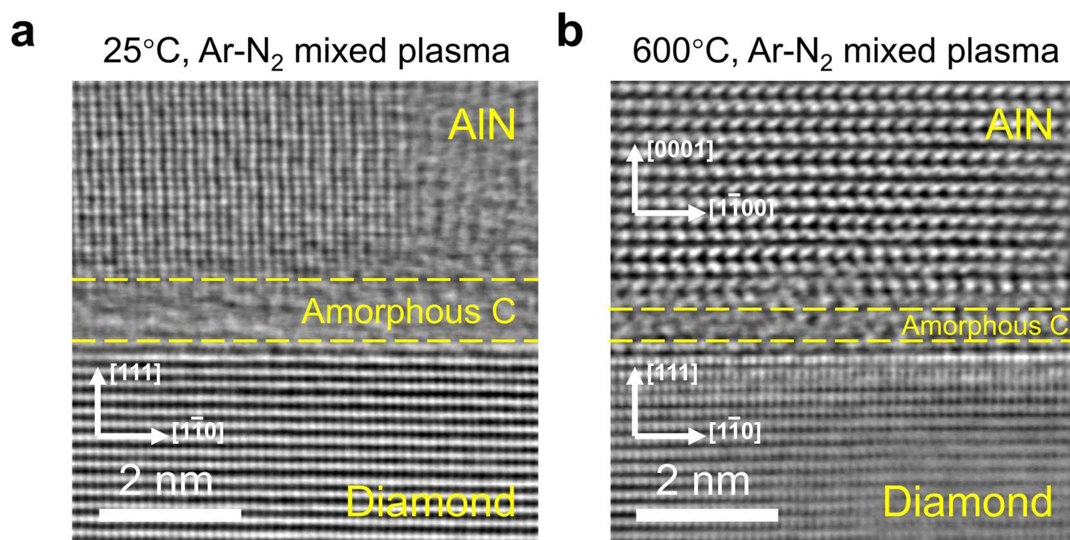

Supplementary Fig. 1 iDPC-STEM images of AlN/Diamond interfaces, with the same Ar-N_2 plasma treatment as in the main text, but under lower temperatures. **a**, 25 °C, with ~1.2 nm-thick interfacial amorphous C layer remaining. **b**, 600 °C, with ~0.6 nm-thick interfacial amorphous C layer remaining.

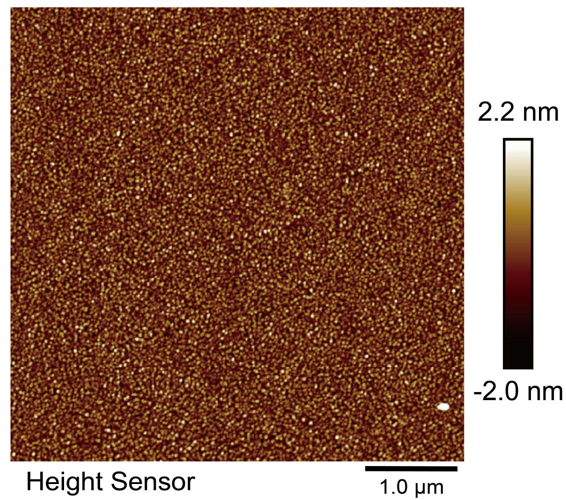

Supplementary Fig. 2 Surface morphology of a representative AlN layer. AFM scanning (5×5 μm^2) reveals a root-mean-square roughness of ~0.67 nm, indicating that the surface is smooth enough to meet the requirements for TDTR and FDTR measurements.

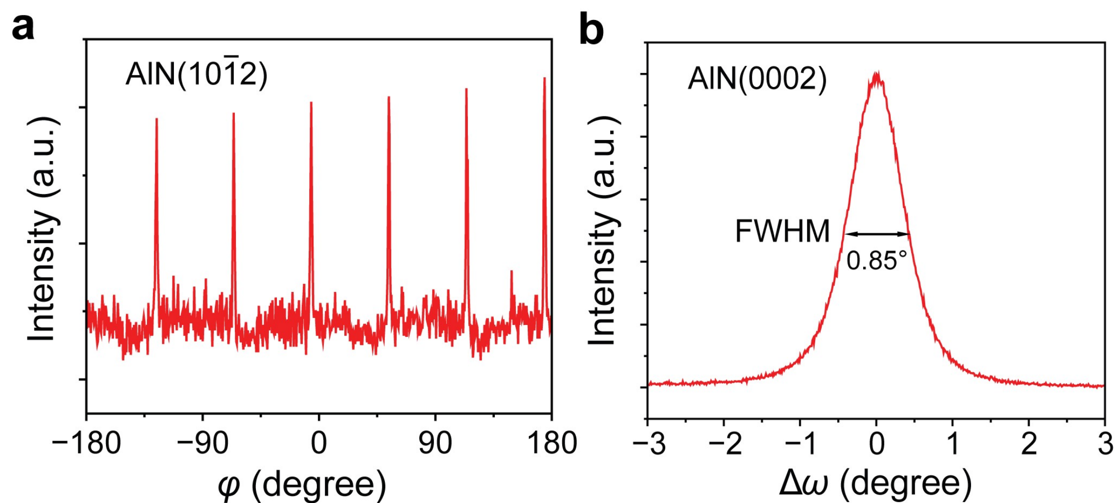

Supplementary Fig. 3 XRD characterizations of the AlN layer obtained by the interfacial atom engineering. a, XRD φ-scan of the AlN (10$\bar{1}$2) reflection. The six pronounced peaks separated by 60° intervals confirm the hexagonal structure and highly uniform in-plane orientation of the AlN layers. **b**, XRD rocking curve for the AlN (0002) plane. The narrow full width at half maximum (FWHM) of 0.85º confirms the high crystalline quality of the AlN layer.

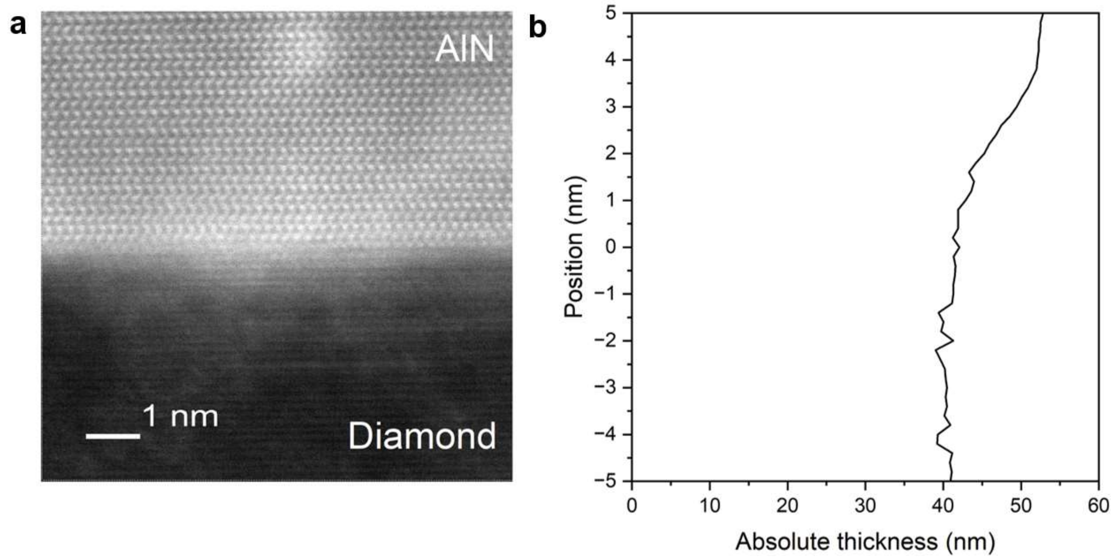

Supplementary Fig. 4 TEM specimen thickness mapping at the AlN/Diamond interface. **a**, An atomically-resolved STEM-HAADF image near the interface. **b**, The thickness mapping results of this area. The specimen thickness, calculated by the log-ratio method, is about 40~55 nm near the interface. The mean free path of a 60 keV electron beam is estimated to be ~70 nm for diamond and ~60 nm for AlN[24]. Therefore, the thickness of the specimen is suitable for the EELS measurement at 60 kV.

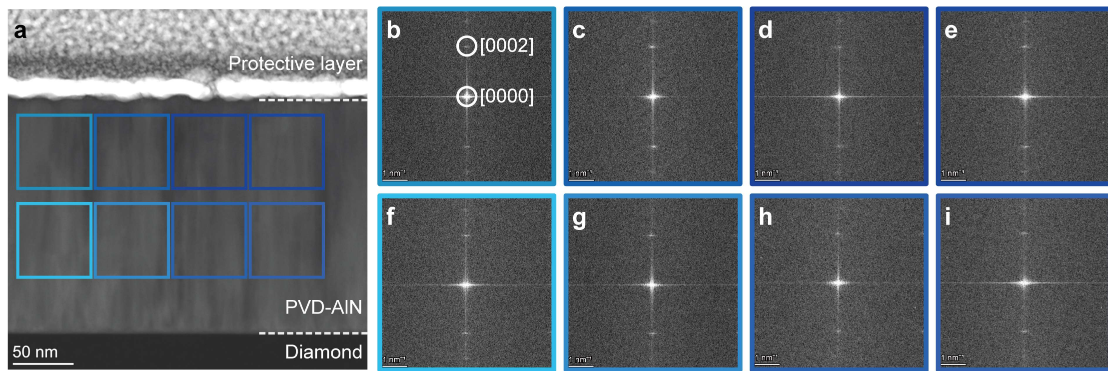

Supplementary Fig. 5 Orientation uniformity in the AlN layers grown on diamond (111) substrate. A cross-sectional TEM image of the PVD AlN/Diamond sample is shown in **a**. Eight different regions were selected for the acquisition of fast Fourier transform (FFT) images, as shown in panels **b**-**i**. The border color of each FFT image corresponds to the respective region in panel (A). The [0002] diffraction spot exhibits nearly identical distance and orientation relative to the [0000] diffraction spot across all FFT images, indicating remarkable uniformity.

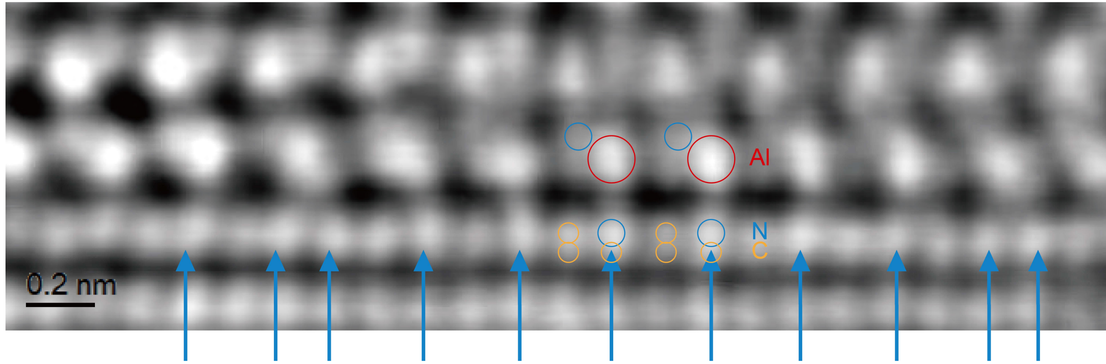

Supplementary Fig. 6 Atomically resolved interface structure of the AlN/Diamond sample. Intensity difference phase contrast scanning transmission electron microscopy (iDPC-STEM) elucidates the atomic structure at the *a*-plane AlN/Diamond interface. The bright spots observed in the upper portion of the figure correspond to Al-N dumbbells within the AlN lattice. The atomic columns directly beneath the Al atoms appear significantly brighter than the surrounding columns, as indicated by the alternating blue arrows. This enhanced brightness suggests an alternating arrangement of C atoms with other atoms. A plausible interpretation is the presence of N atoms in these columns, suggesting that some C atoms on the diamond surface have been replaced by N atoms.

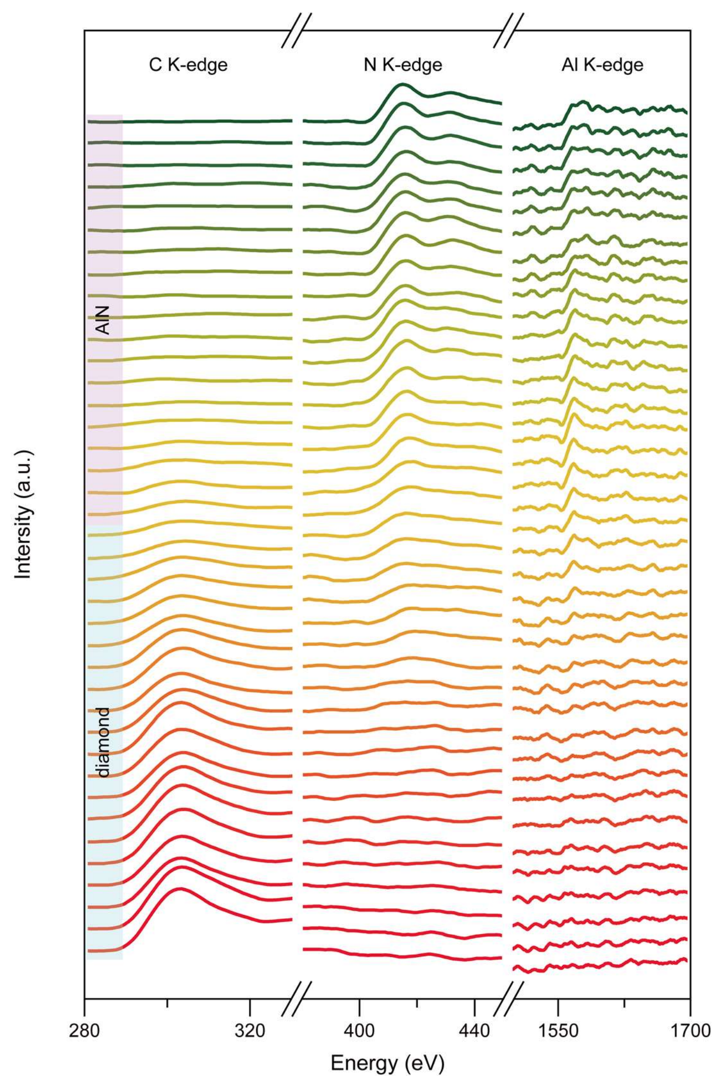

Supplementary Fig. 7 Atomically resolved element mapping across the AlN/Diamond interface. Core-loss electron energy-loss spectroscopy elemental maps for carbon (C K-edge, left), nitrogen (N K-edge, middle), and aluminum (Al K-edge, right). Each stack is presented with a spatial step of 0.05 nm. Fig. 2e is derived from the data presented in this figure.

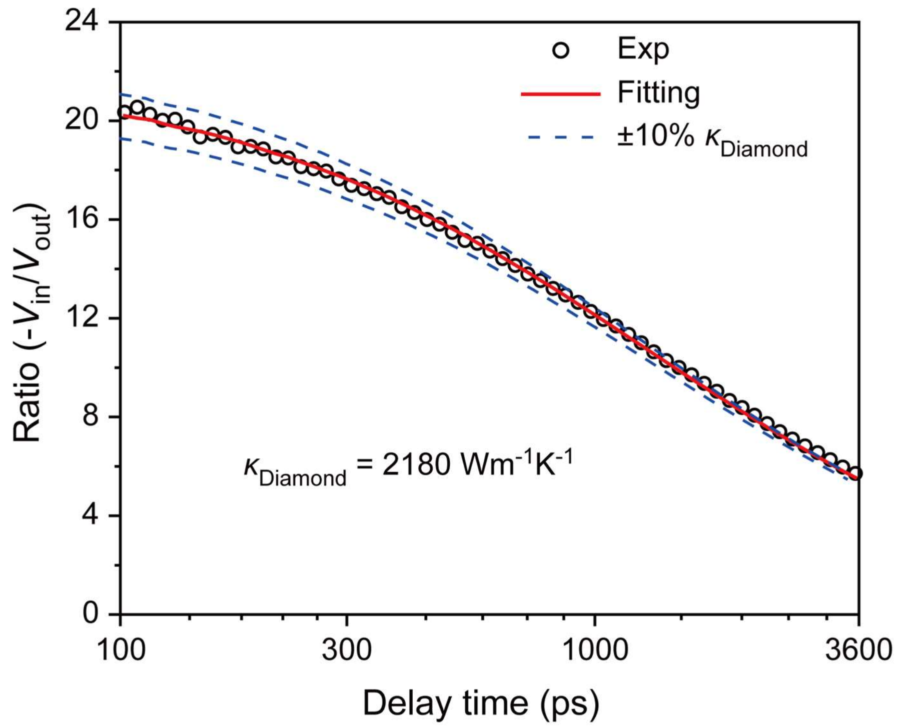

Supplementary Fig. 8 Representative TDTR data for the bulk diamond substrate. Measured data (black circles) and fitted curve (red solid line) of the Al/Diamond sample at room temperature. The upper and lower blue dashed lines represent the signals if the thermal conductivity of the diamond substrate ($\kappa_{\mathrm{Diamond}}$) differs from the best-fit value by 10%, indicating that $\kappa_{\mathrm{Diamond}}$ exhibits good sensitivity to such variations.

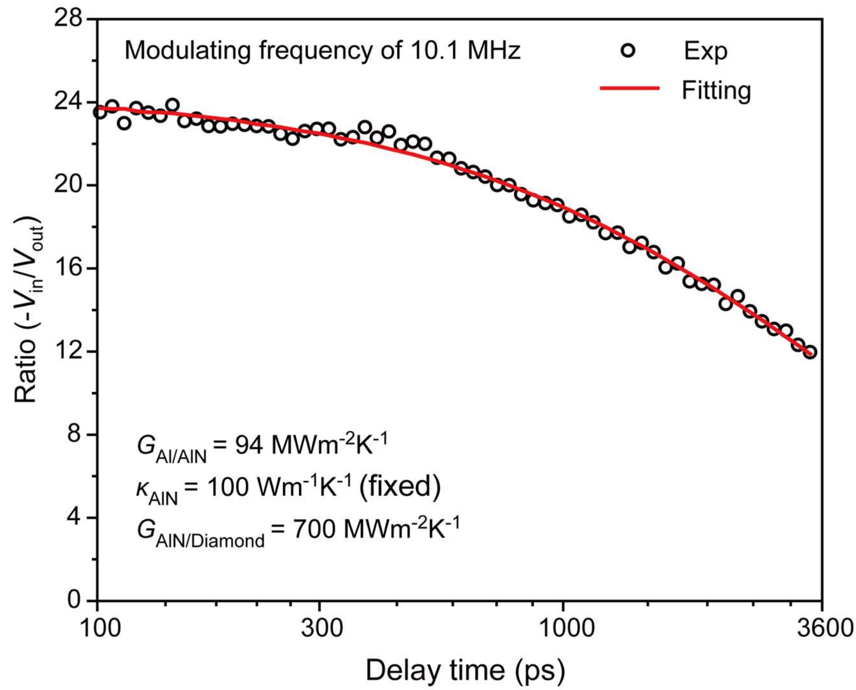

Supplementary Fig. 9 Representative TDTR data for an AlN/Diamond sample with 230 nm AlN, where κ_{AlN} is assumed to be 100 Wm^{-1}K^{-1}. Measured data (circles) and fitted curve (solid line) of the sample at room temperature. The lower bound of $G_{AlN/Diamond}$ was estimated by fixing κ_{AlN} to an upper bound of 100 Wm^{-1}K^{-1}, and the fitting results suggested that $G_{AlN/Diamond}$ should be no less than 700 MWm^{-2}K^{-1}.

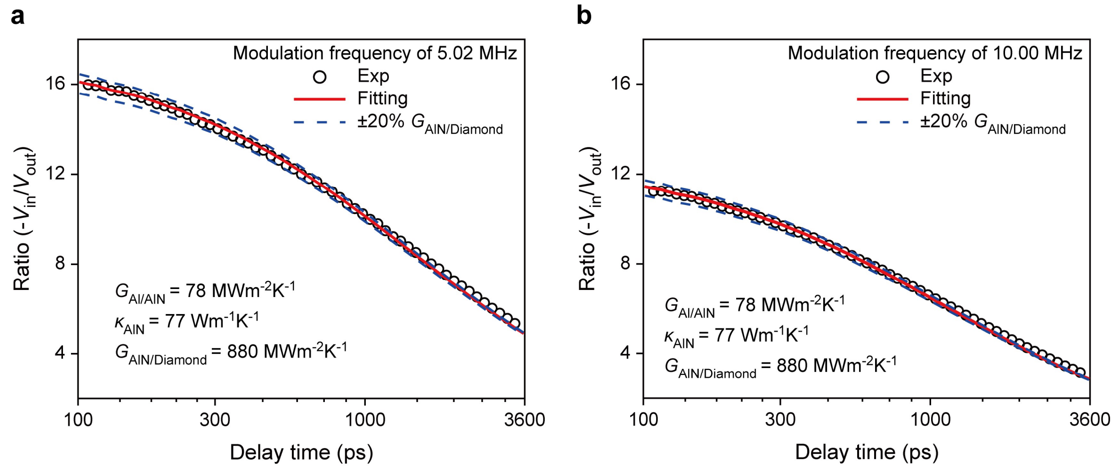

Supplementary Fig. 10 Representative TDTR data for an AlN/Diamond sample with 230 nm AlN at the modulation frequencies of (a) 5.02 MHz and (b) 10.00 MHz. Measured data (circles) and fitted curve (solid line) of the sample at room temperature. The upper and lower blue dashed lines represent the signals if $G_{\text{AlN/Diamond}}$ differs from the best-fit value by 20%, indicating that $G_{\text{AlN/Diamond}}$ has good sensitivity.

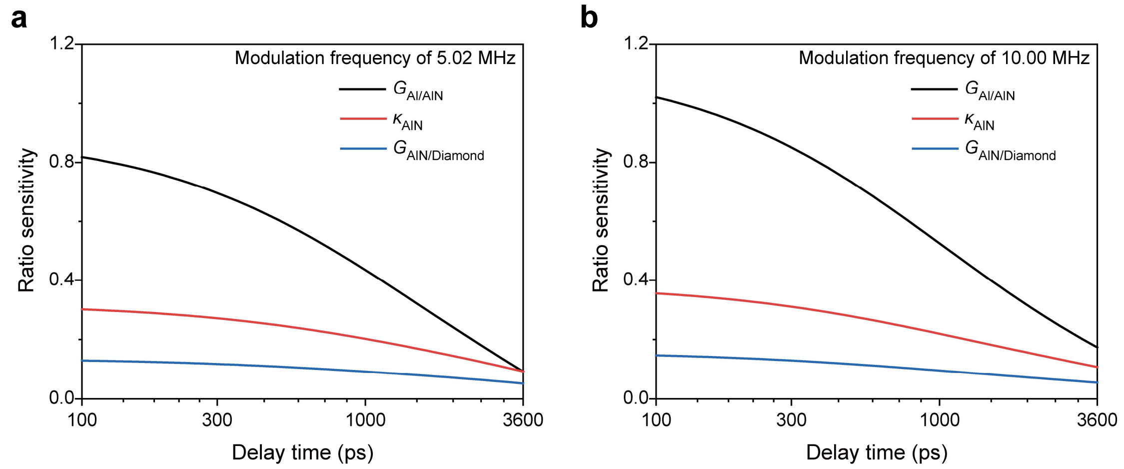

Supplementary Fig. 11 Sensitivity analysis of the TDTR measurements for an AlN/Diamond sample with 230 nm AlN. a,b, The signal sensitivity with respect to $G_{\mathrm{Al/AlN}}$, κ_{AlN}, and $G_{\mathrm{AlN/Diamond}}$ at the modulation frequency of (**a**) 5.02 MHz and (**b**) 10.00 MHz.

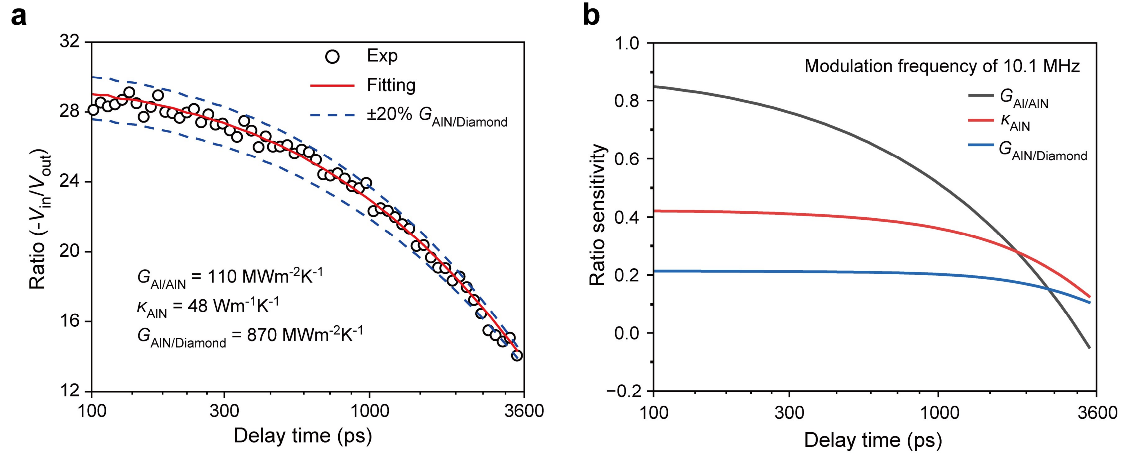

Supplementary Fig. 12 Representative TDTR data for an AlN/Diamond sample with 150 nm AlN layer. a, Measured data (circles) and fitted curve (solid line) of the sample at room temperature. The upper and lower blue dashed lines represent the signals if $G_{\mathrm{AlN/Diamond}}$ differs from the best-fit value by 20%, indicating that $G_{\mathrm{AlN/Diamond}}$ has good sensitivity. **b**, The signal sensitivity with respect to $G_{\mathrm{Al/AlN}}$, κ_{AlN}, and $G_{\mathrm{AlN/Diamond}}$ at the modulation frequency of 10.1 MHz.

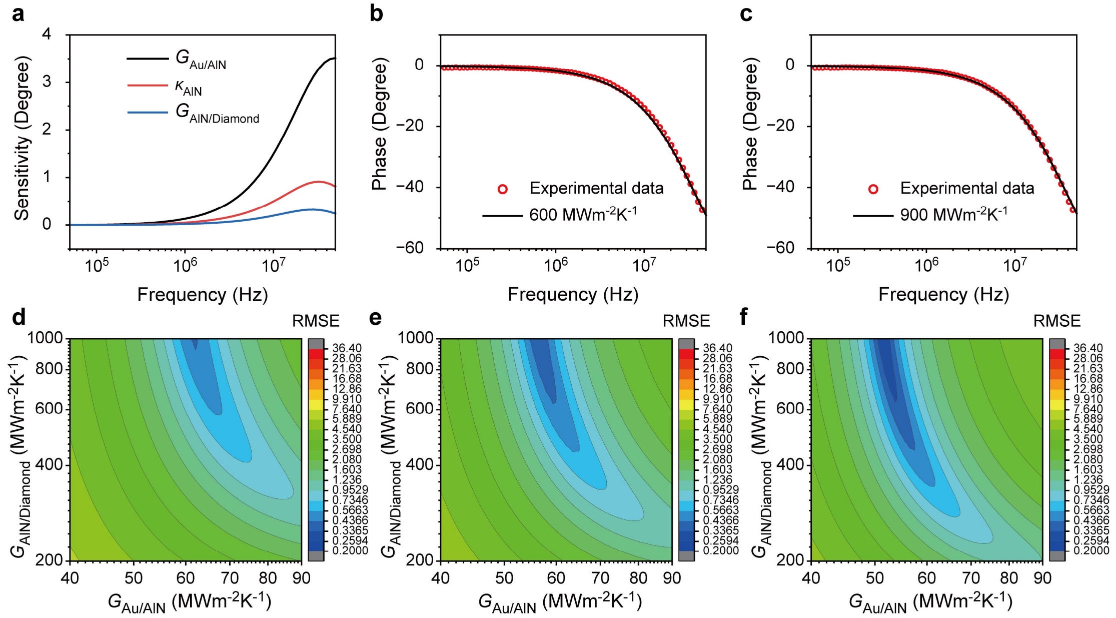

Supplementary Fig. 13 Sensitivity and uncertainty analysis for the FDTR measurements. **a**, Calculated sensitivity to $G_{Au/AlN}$, κ_{AlN}, and $G_{AlN/Diamond}$. **b**,**c**, Comparison of the measured data with the fitted curve when $G_{AlN/Diamond}$ takes the value of (**b**) 600 MWm^{-2}K^{-1} and (**c**) 900 MWm^{-2}K^{-1}. **d**-**f**, Contour maps of the root-mean-square error (RMSE) between the measured and fitted data for three different values of κ_{AlN}, including (**d**) 50 Wm^{-1}K^{-1}, (**e**) 65 Wm^{-1}K^{-1}, and (**f**) 100 Wm^{-1}K^{-1}.

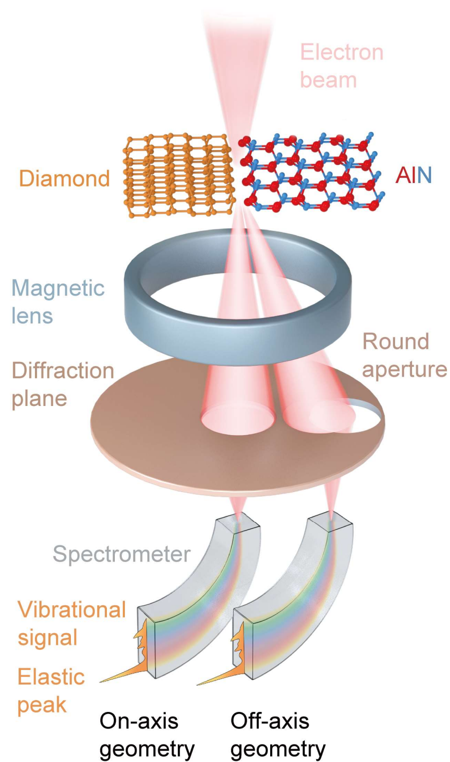

Supplementary Fig. 14 Schematic of the monochromated STEM-EELS setup in the main text. A precisely focused electron beam with a probe diameter of less than 0.1 nm and a kinetic energy of 60 kV scans the sample and undergoes inelastic scattering with the lattice vibrations. This generates an energy loss spectrum typically confined to the <200 meV range, which is directly correlated with the local PDOS.

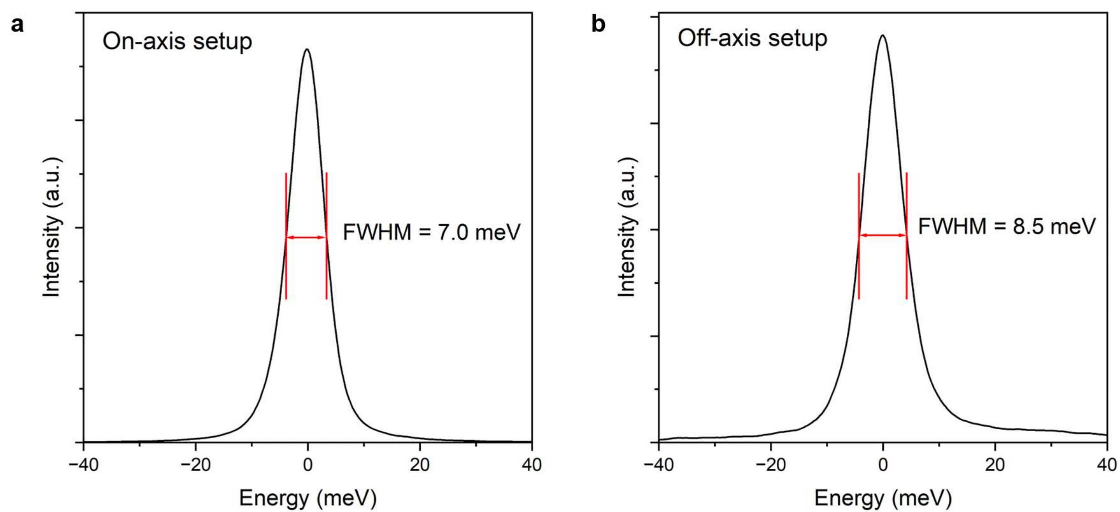

Supplementary Fig. 15 Energy resolution achieved in the EELS mappings. The energy resolution in the EELS measurements is typically characterized as the full-width at half-maximum (FWHM) of the zero-loss peak (ZLP). **a**,**b**, The best energy resolution achieved was approximately (**a**) 7.0 meV for the on-axis setup and (**b**) 8.5 meV for the off-axis setup when the electron beam was focused on the specimen.

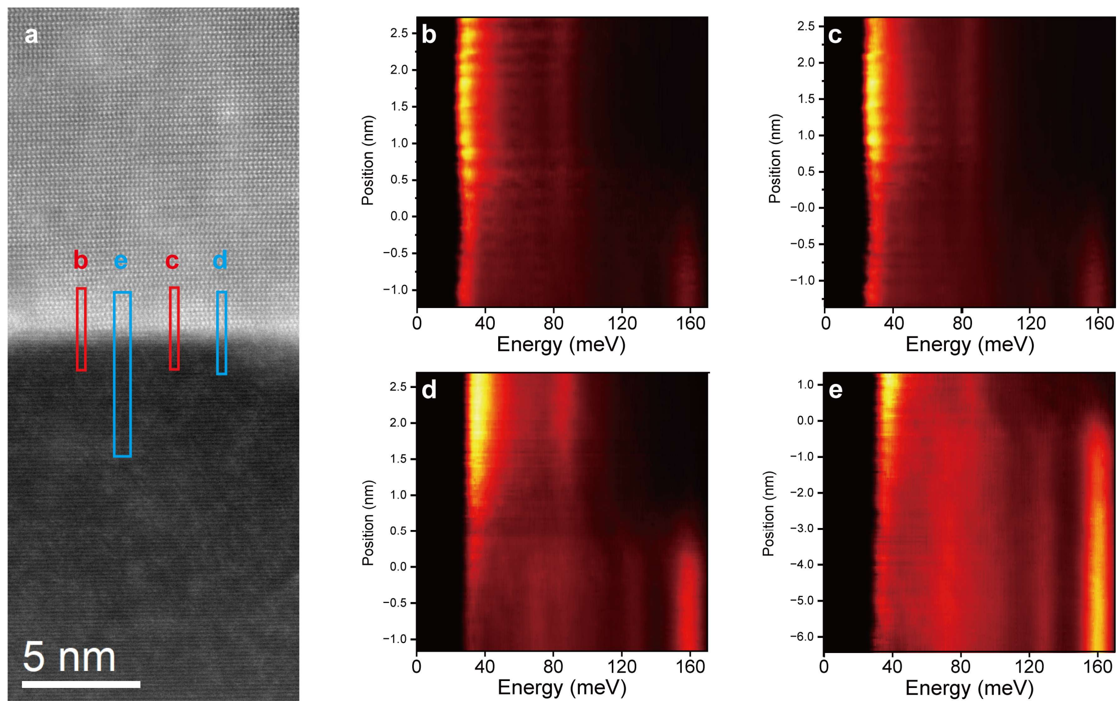

Supplementary Fig. 16 EELS data acquired across the AlN/Diamond interface with different experimental configurations and in different regions. a, A low-magnification HAADF image showing the regions where the datasets were acquired. The boxes labeled **b** to **e** mark the four regions for data acquisition, corresponding to panels **b** to **e**. EELS line profiles under (**b**,**c**) on-axis geometry and (**d**,**e**) off-axis geometry acquired using different pixel sizes and in different scanning regions, with other experimental conditions unchanged. All datasets give consistent results as the one shown in Fig. 4a,b.

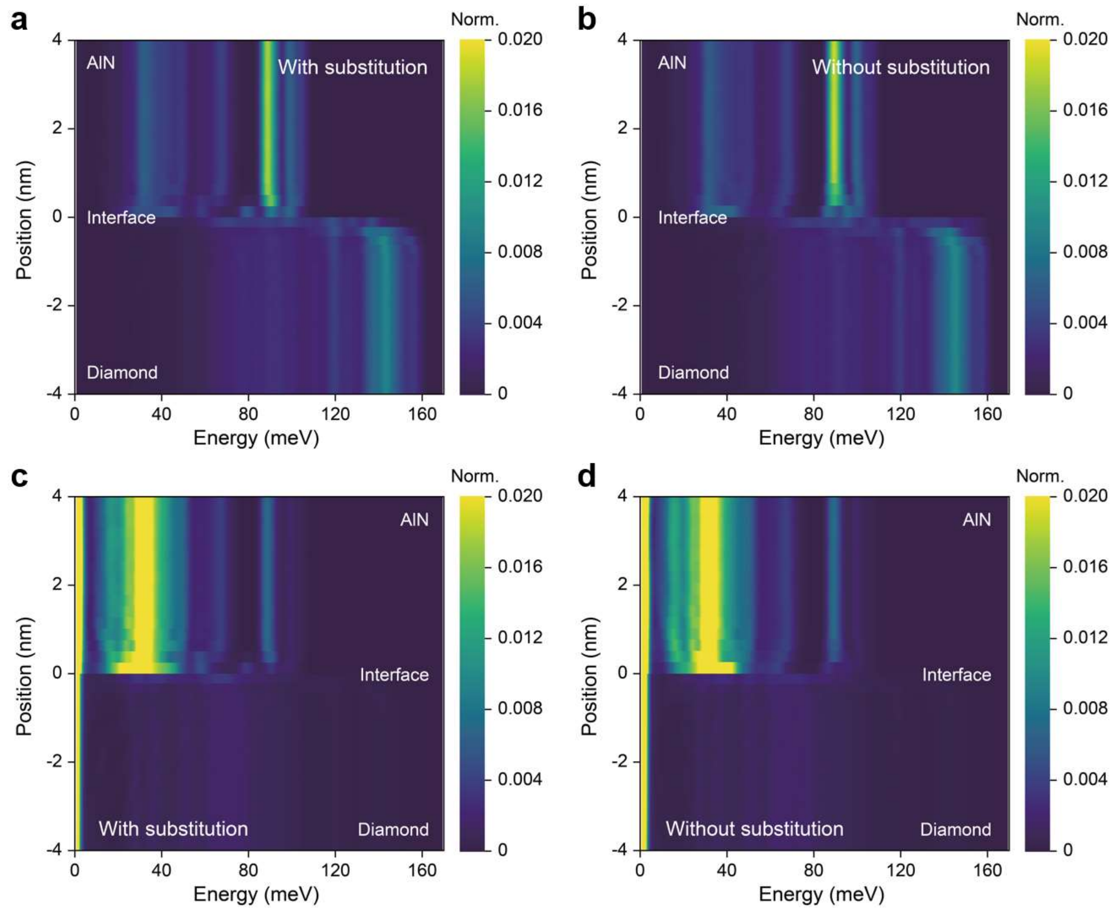

Supplementary Fig. 17 Position-dependent normalized PDOS with and without accounting for phonon population. a,**b**, Normalized PDOS across the AlN/Diamond interface (**a**) with and (**b**) without N_C, without considering the phonon population. **c**,**d**, Corresponding results considering the phonon population given by the Bose-Einstein distribution at 300 K.

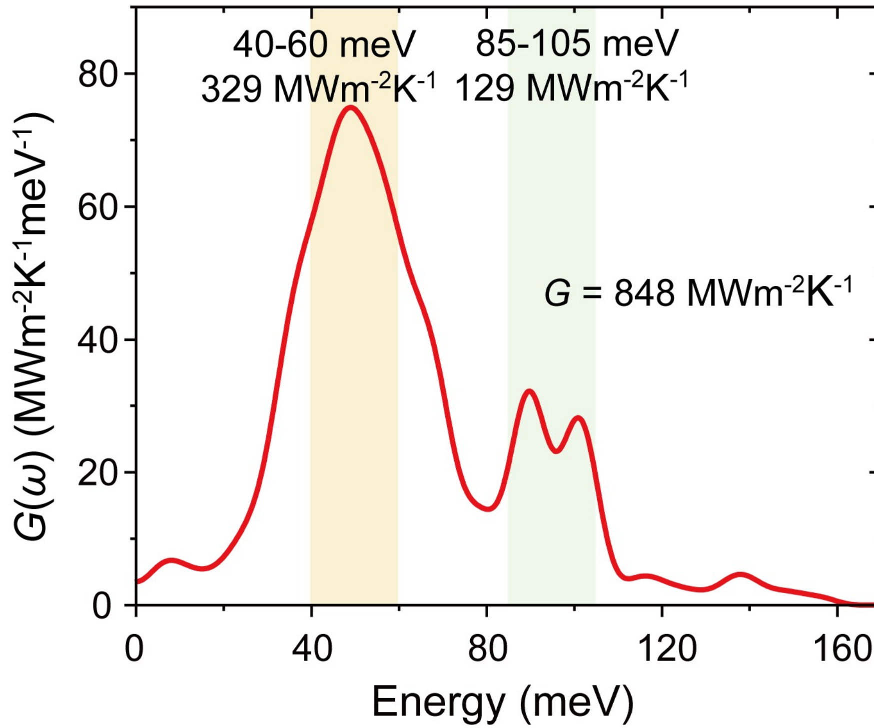

Supplementary Fig. 18 Calculated spectral thermal conductance [$G(\omega)$] at the interface corresponding to Fig. 4d. The yellow and green bands highlight the two energy ranges with major contributions to $G(\omega)$. The phonons in the 40-60 meV range, which mainly consist of AlN-TA/LA/TO modes and diamond-BEH, contribute 39% of the total thermal conductance. In addition, the matched AlN-TO/LO and diamond-TA modes in the 85-105 meV range account for ~15%. This curve is the same as the solid red curve in Fig. 5a but is replotted here to better show the energy ranges for integration and the relative contribution to G.

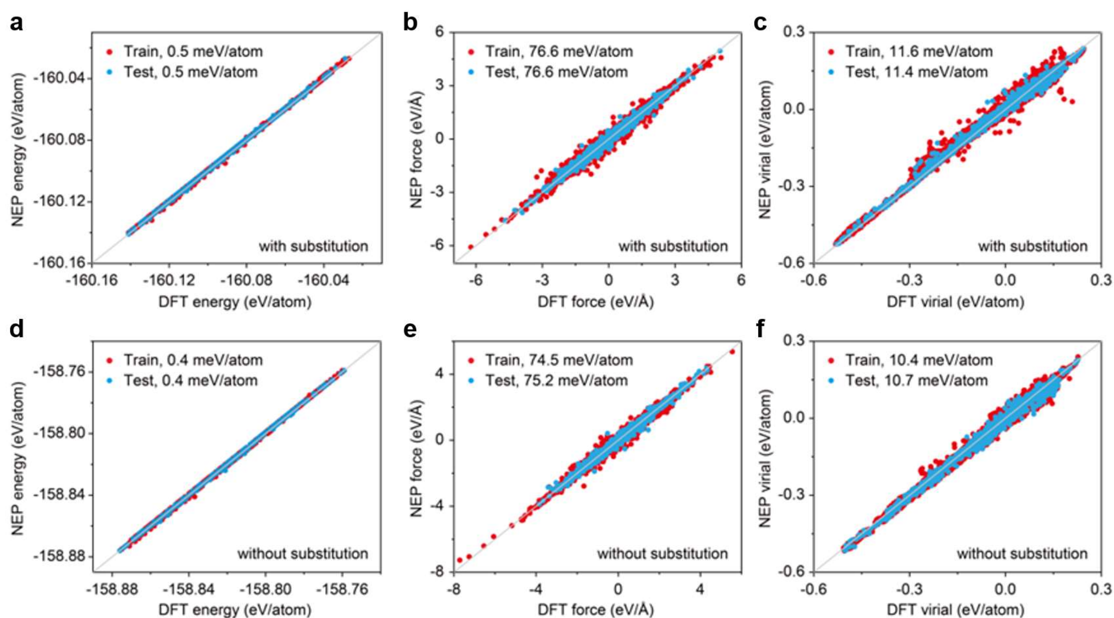

Supplementary Fig. 19 Parity plots of energy, force, and virial stress for different models. a-**f**, Comparison of energy, force, and virial stress between the NEP predictions and DFT references for models (**a**-**c**) with and (**d**-**f**) without N_C. The root-mean-square errors (RMSE) for both the training and test datasets are provided at the top left corner of each panel.

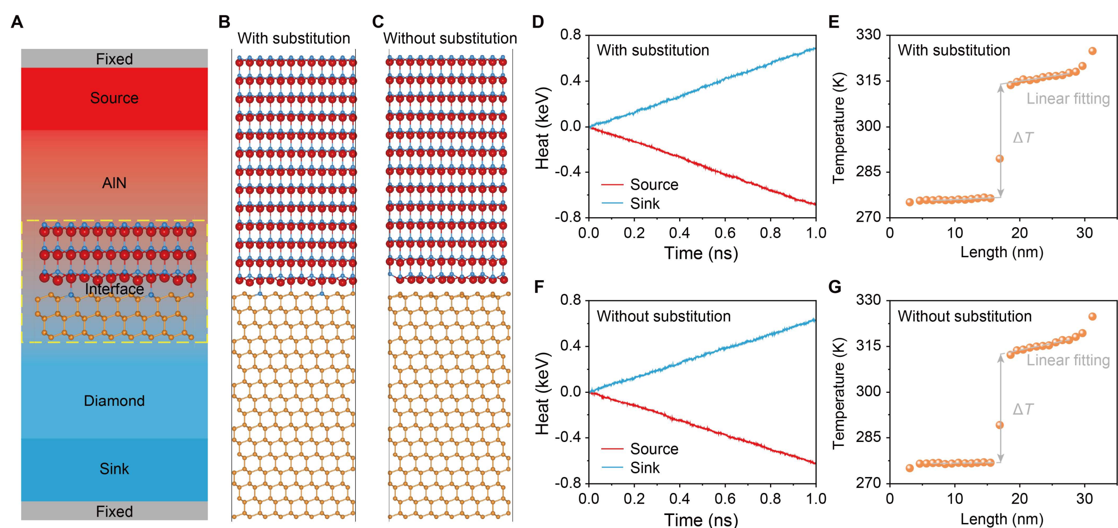

Supplementary Fig. 20 NEMD simulation for calculating the interfacial thermal conductance. a, Schematic illustration of the model for the NEMD simulations. **b**,**c**, Atomic structures for models (**b**) with and (**c**) without N_C. **d**-**g**, The accumulated energies in the thermostats and the temperature profiles for the models (**d**,**e**) with and (**f**,**g**) without N_C at 300 K.

Supplementary Tables

Supplementary Table 1 Fitting parameters for the TDTR data in Fig. 3b.

Layer	C_p ($MJm^{-3}K^{-1}$)	κ ($Wm^{-1}K^{-1}$)	Thickness (nm)	G ($MWm^{-2}K^{-1}$)
Al	2.42	170	80	/
Al/AlN interface	0.1	/	/	Fit
AlN	2.44	Fit	225	/
AlN/Diamond interface	0.1	/	/	Fit
Diamond	1.75	2180	1000 (Infinity)	/

Supplementary Table 2 Fitting parameters for the TDTR data in Supplementary Fig. 9.

Layer	C_p ($MJm^{-3}K^{-1}$)	κ ($Wm^{-1}K^{-1}$)	Thickness (nm)	G ($MWm^{-2}K^{-1}$)
Al	2.42	170	80	/
Al/AlN interface	0.1	/	/	Fit
AlN	2.44	Fit	150	/
AlN/Diamond interface	0.1	/	/	Fit
Diamond	1.75	2180	1000 (Infinity)	/

Supplementary Table 3 Fitting parameters for the FDTR data in Fig. 3c.

Layer	C_p ($MJm^{-3}K^{-1}$)	κ ($Wm^{-1}K^{-1}$)	Thickness (nm)	G ($MWm^{-2}K^{-1}$)
Au	2.48	149	70	/
Au/AlN interface	/	/	/	Fit
AlN	2.4	Fit	225	/
AlN/Diamond interface	/	/	/	Fit
Diamond	1.79	2170	1000 (Infinity)	/

Supplementary Table 4 Interfacial thermal conductance values experimentally achieved between diamond and various semiconductors which are plotted in Fig. 3d.

Interface	G ($MWm^{-2}K^{-1}$)	Reference
Diamond/Si	90.9	[25]
Diamond/Si	100	[26]
Diamond/Si	50 +27/-13	[27]
Diamond/Si	63.7	[28]
Diamond/Si	80	[28]
Diamond/Si	105	[28]
Diamond/Si	>500	[29]
Diamond/Si	>200	[29]
Diamond/Si	142	[29]
Diamond/SiC	55	[30]
Diamond/SiC	529	[31]
Diamond/SiC	322	[31]
Diamond/SiC	93	[32]
Diamond/GaAs	40	[33]
Diamond/GaN	27.78 +13.89/-6.94	[34]
Diamond/GaN	55.56	[35]
Diamond/GaN	34.5	[36]
Diamond/GaN	27.78	[37]
Diamond/GaN	37.4 +4.63/-3.70	[37]
Diamond/GaN	83.33 +16.67/-11.90	[38]
Diamond/GaN	31.45 +6.29/-4.49	[39]
Diamond/GaN	57.47 +11.97/-8.45	[39]
Diamond/GaN	153.85	[40]
Diamond/GaN	54.95 +13.55/-4.18	[41]
Diamond/GaN	105.26 +22.94/-30.07	[41]

Interface	G ($MWm^{-2}K^{-1}$)	Reference
Diamond/GaN	53	[42]
Diamond/GaN	92	[42]
Diamond/GaN	33.33+6.67-4.76	[43]
Diamond/GaN	167	[44]
Diamond/GaN	90	[45]
Diamond/GaN	322.58 +94.09/-59.42	[46]
Diamond/GaN	28	[47]
Diamond/GaN	32.4	[47]
Diamond/GaN	71.3	[47]
Diamond/GaN	85.9	[47]
Diamond/GaN	25.41	[48]
Diamond/GaN	38.46 +24.04/-10.68	[49]
Diamond/GaN	200	[29]
Diamond/GaN	120	[50]
Diamond/AlN	62.5	[51]
Diamond/Ga_2O_3	179	[52]
Diamond/Ga_2O_3	136	[52]
Diamond/Ga_2O_3	139	[52]
Diamond/Ga_2O_3	33.1 +2.0/-1.9	[53]
Diamond/Ga_2O_3	60.9±3.0	[54]
Diamond/Ga_2O_3	46.1±2.3	[54]
Diamond/Ga_2O_3	127.06	[55]

References:

1. Schmidt, A., Chiesa, M., Chen, X. & Chen, G. An optical pump-probe technique for measuring the thermal conductivity of liquids. *Rev. Sci. Instrum.* **79**, 064902 (2008).

2. Kang, K., Koh, Y.K., Chiritescu, C., Zheng, X. & Cahill, D.G. Two-tint pump-probe measurements using a femtosecond laser oscillator and sharp-edged optical filters. *Rev. Sci. Instrum.* **79**, 114901 (2008).

3. Wei, L., Kuo, P.K., Thomas, R.L., Anthony, T.R. & Banholzer, W.F. Thermal conductivity of isotopically modified single crystal diamond. *Phys. Rev. Lett.* **70**, 3764-3767 (1993).

4. Tian, F. *et al.* Unusual high thermal conductivity in boron arsenide bulk crystals. *Science* **361**, 582-585 (2018).

5. Onn, D.G., Witek, A., Qiu, Y.Z., Anthony, T.R. & Banholzer, W.F. Some aspects of the thermal conductivity of isotopically enriched diamond single crystals. *Phys. Rev. Lett.* **68**, 2806-2809 (1992).

6. Xu, R.L. *et al.* Thermal conductivity of crystalline AlN and the influence of atomic-scale defects. *J. Appl. Phys.* **126**, 185105 (2019).

7. Costescu, R.M., Wall, M.A. & Cahill, D.G. Thermal conductance of epitaxial interfaces. *Phys. Rev. B* **67**, 054302 (2003).

8. Koh, Y.R. *et al.* Bulk-like Intrinsic Phonon Thermal Conductivity of Micrometer-Thick AlN Films. *ACS Appl. Mater. Interfaces* **12**, 29443-29450 (2020).

9. Kühne, T.D. *et al.* CP2K: An electronic structure and molecular dynamics software package - Quickstep: Efficient and accurate electronic structure calculations. *J. Chem. Phys.* **152**, 194103 (2020).

10. Perdew, J.P., Burke, K. & Ernzerhof, M. Generalized Gradient Approximation Made Simple. *Phys. Rev. Lett.* **77**, 3865-3868 (1996).

11. VandeVondele, J. & Hutter, J. Gaussian basis sets for accurate calculations on molecular systems in gas and condensed phases. *J. Chem. Phys.* **127**, 114105 (2007).

12. Goedecker, S., Teter, M. & Hutter, J. Separable dual-space Gaussian pseudopotentials. *Phys. Rev. B* **54**, 1703-1710 (1996).

13. Grimme, S., Antony, J., Ehrlich, S. & Krieg, H. A consistent and accurate ab initio parametrization of density functional dispersion correction (DFT-D) for the 94 elements H-Pu. *J. Chem. Phys.* **132**, 154104 (2010).

14. Grimme, S., Ehrlich, S. & Goerigk, L. Effect of the damping function in dispersion corrected density functional theory. *J. Comput. Chem.* **32**, 1456-1465 (2011).

15. Fan, Z. *et al.* Neuroevolution machine learning potentials: Combining high accuracy and low cost in atomistic simulations and application to heat transport. *Phys. Rev. B* **104**, 104309 (2021).

16. Fan, Z. Improving the accuracy of the neuroevolution machine learning potential for multi-component systems. *J. Phys.: Condens. Matter* **34**, 125902 (2022).

17. Dong, H. *et al.* Molecular dynamics simulations of heat transport using machine-learned potentials: A mini-review and tutorial on GPUMD with neuroevolution potentials. *J. Appl. Phys.* **135**, 161101 (2024).

18. Fan, Z., Chen, W., Vierimaa, V. & Harju, A. Efficient molecular dynamics simulations with many-body potentials on graphics processing units. *Comput. Phys. Commun.* **218**, 10-16 (2017).

19. Fan, Z. *et al.* GPUMD: A package for constructing accurate machine-learned potentials and performing highly efficient atomistic simulations. *J. Chem. Phys.* **157**, 114801 (2022).

20. Xu, K. *et al.* GPUMD 4.0: A high-performance molecular dynamics package for versatile materials simulations with machine-learned potentials. *Mater. Genome Eng. Adv.* **3**, e70028 (2025).

21. Shi, R. *et al.* Atomic-scale observation of localized phonons at FeSe/$SrTiO_3$ interface. *Nat. Commun.* **15**, 3418 (2024).

22. Qi, R.S. *et al.* Measuring phonon dispersion at an interface. *Nature* **599**, 399-403 (2021).

23. Yang, H. *et al.* Phonon modes and electron-phonon coupling at the FeSe/$SrTiO_3$ interface. *Nature* **635**, 332-336 (2024).

24. Egerton, R. *Electron Energy Loss Spectroscopy in the Electron Microscope (Plenum, New York, 1986) pp.294-300.*

25. Verhoeven, H., Rei\S, H., Fü\Ser, H.J. & Zachai, R. Thermal resistance of thin diamond films deposited at low temperatures. *Appl. Phys. Lett.* **69**, 1562-1564 (1996).

26. Goyal, V., Subrina, S., Nika, D.L. & Balandin, A.A. Reduced thermal resistance of the silicon-synthetic diamond composite substrates at elevated temperatures. *Appl. Phys. Lett.* **97**, 031904 (2010).

27. Mohr, M. *et al.* Influence of grain boundaries on elasticity and thermal conductivity of nanocrystalline diamond films. *Acta Mater.* **122**, 92-98 (2017).

28. Cheng, Z. *et al.* Tunable Thermal Energy Transport across Diamond Membranes and Diamond-Si Interfaces by Nanoscale Graphoepitaxy. *ACS Appl. Mater. Interfaces* **11**, 18517-18527 (2019).

29. Malakoutian, M. *et al.* Lossless Phonon Transition Through GaN‐Diamond and Si‐Diamond Interfaces. *Adv. Electron. Mater.* **11**, 2400146 (2024).

30. Kagawa, R. *et al.* High Thermal Stability and Low Thermal Resistance of Large Area GaN/3C-SiC/Diamond Junctions for Practical Device Processes. *Small* **20**, 2305574 (2024).

31. Woo, K. *et al.* Interlayer Engineering to Achieve <1 m^2K/GW Thermal Boundary Resistances to Diamond for Effective Device Cooling. *IEDM*, 1-4 (2023).

32. Kagawa, R., Ohno, Y., Nagai, Y., Shigekawa, N. & Liang, J. Fabrication of low thermal resistance 3C-SiC/diamond structure for GaN epitaxial layer growth. *Funct. Diamond* **4**, 2337352 (2024).

33. Clark, S.P.R. *et al.* Growth and thermal conductivity analysis of polycrystalline GaAs on chemical vapor deposition diamond for use in thermal management of high-power semiconductor lasers. *J. Vac. Sci. Technol. B* **29**, 03C130 (2011).

34. Cho, J. *et al.* Improved Thermal Interfaces of GaN–Diamond Composite Substrates for HEMT Applications. *IEEE Trans. Compon. Pack. Manuf. Technol.* **3**, 79-95 (2013).

35. Dumka, D.C. *et al.* Electrical and Thermal Performance of AlGaN/GaN HEMTs on Diamond Substrate for RF Applications. *IEEE CSICS*, 1-4 (2013).

36. Altman, D. *et al.* Analysis and characterization of thermal transport in GaN HEMTs on Diamond substrates. *IEEE ITHERM*, 1199-1205 (2014).

37. Pomeroy, J.W., Bernardoni, M., Dumka, D.C., Fanning, D.M. & Kuball, M. Low thermal resistance GaN-on-diamond transistors characterized by three-dimensional Raman thermography mapping. *Appl. Phys. Lett.* **104**, 083513 (2014).

38. Sun, H. *et al.* Reducing GaN-on-diamond interfacial thermal resistance for high power transistor applications. *Appl. Phys. Lett.* **106**, 111906 (2015).

39. Cho, J., Francis, D., Altman, D.H., Asheghi, M. & Goodson, K.E. Phonon conduction in GaN-diamond composite substrates. *J. Appl. Phys.* **121**, 055105 (2017).

40. Zhou, Y. *et al.* Barrier-Layer Optimization for Enhanced GaN-on-Diamond Device Cooling. *ACS Appl. Mater. Interfaces* **9**, 34416-34422 (2017).

41. Yates, L. *et al.* Low Thermal Boundary Resistance Interfaces for GaN-on-Diamond Devices. *ACS Appl. Mater. Interfaces* **10**, 24302-24309 (2018).

42. Cheng, Z., Mu, F., Yates, L., Suga, T. & Graham, S. Interfacial Thermal Conductance across Room-Temperature-Bonded GaN/Diamond Interfaces for GaN-on-Diamond Devices. *ACS Appl. Mater. Interfaces* **12**, 8376-8384 (2020).

43. Field, D.E. *et al.* Crystalline Interlayers for Reducing the Effective Thermal Boundary Resistance in GaN-on-Diamond. *ACS Appl. Mater. Interfaces* **12**, 54138-54145 (2020).

44. Smith, E.J.W. *et al.* Mixed-size diamond seeding for low-thermal-barrier growth of CVD diamond onto GaN and AlN. *Carbon* **167**, 620-626 (2020).

45. Cheng, Z., Goorsky, M., Mu, F., Suga, T. & Graham, S. Creating Low Thermal Resistance Interfaces in Wide Bandgap Semiconductors Through Bonding. *IEEE ICSJ*, 135-137 (2021).

46. Malakoutian, M. *et al.* Record-Low Thermal Boundary Resistance between Diamond and GaN-on-SiC for Enabling Radiofrequency Device Cooling. *ACS Appl. Mater. Interfaces* **13**, 60553-60560 (2021).

47. Mu, F. *et al.* A novel strategy for GaN-on-diamond device with a high thermal boundary conductance. *J. Alloy. Compd.* **905**, 164076 (2022).

48. Wu, M. *et al.* Structural and thermal analysis of polycrystalline diamond thin film grown on GaN-on-SiC with an interlayer of 20 nm PECVD-SiN. *Appl. Phys. Lett.* **120**, 121603 (2022).

49. Wang, Y. *et al.* Effect of bias-enhanced nucleation on the microstructure and thermal boundary resistance of GaN/SiNx/diamond multilayer composites. *Mater. Charact.* **201**, 112985 (2023).

50. Xu, B. *et al.* Record-Low thermal boundary resistance at bonded GaN/diamond interface by controlling ultrathin heterogeneous amorphous layer. *Acta Mater.* **282**, 120458 (2025).

51. Mandal, S. *et al.* Thick, Adherent Diamond Films on AlN with Low Thermal Barrier Resistance. *ACS Appl. Mater. Interfaces* **11**, 40826-40834 (2019).

52. Cheng, Z. *et al.* Integration of polycrystalline Ga2O3 on diamond for thermal management. *Appl. Phys. Lett.* **116**, 062105 (2020).

53. Malakoutian, M. *et al.* Polycrystalline diamond growth on β-Ga_2O_3 for thermal management. *Appl. Phys. Express* **14**, 055502 (2021).

54. Gu, L. *et al.* A strategy for enhancing interfacial thermal transport in Ga_2O_3-diamond composite structure by introducing an AlN interlayer. *Nano Energy* **132**, 110389 (2024).

55. Gu, L. *et al.* The Influence of Annealing Temperature on the Interfacial Heat Transfer in Pulsed Laser Deposition-Grown Ga_2O_3 on Diamond Composite Substrates. *C-J. Carbon Res.* **10**, 80 (2024).